Dynamic Potential Sputtering of Lunar Analogue Material by Solar Wind Ions

Paul S. Szabo[a,*], Herbert Biber[a], Noah Jäggi[b], Matthias Brenner[a], David Weichselbaum[a], Anna Niggas[a], Reinhard Stadlmayr[a], Andreas Mutzke[c], Andreas Nenning[d], Markus Sauer[e], Daniel Primetzhofer[f], Jürgen Fleig[d], Annette Foelske-Schmitz[e], Klaus Mezger[g], Helmut Lammer[h], André Galli[b], Peter Wurz[b], and Friedrich Aumayr[a,*]

[a] *Institute of Applied Physics, TU Wien, Wiedner Hauptstraße 8-10, 1040 Vienna, Austria*

[b] *Physics Institute, University of Bern, Sidlerstrasse 5, 3012 Bern, Switzerland*

[c] *Max-Planck-Institut für Plasmaphysik, Wendelsteinstraße 1, 17491 Greifswald, Germany*

[d] *Institute of Chemical Technologies and Analytics, TU Wien, Getreidemarkt 9, 1060 Vienna, Austria*

[e] *Analytical Instrumentation Center, TU Wien, Getreidemarkt 9, 1060 Vienna, Austria*

[f] *Department of Physics and Astronomy, Uppsala University, Ångströmlaboratoriet, Lägerhyddsvägen 1, 752 37 Uppsala, Sweden*

[g] *Institute of Geological Sciences, University of Bern, Baltzerstraße 1+3, 3012 Bern, Switzerland*

[h] *Space Research Institute (IWF), Austrian Academy of Sciences, Schmiedlstr. 6, 8042 Graz, Austria*

[*]Corresponding authors : szabo@iap.tuwien.ac.at, aumayr@iap.tuwien.ac.at

Abstract

Pyroxenes $((Ca, Mg, Fe, Mn)_2Si_2O_6)$ belong to the most abundant rockforming minerals that make up the surface of rocky planets and moons. Therefore sputtering of pyroxenes by solar wind ions has to be considered as a very important process for modifying the surface of planetary bodies. In order to quantify this effect, sputtering of wollastonite $(CaSiO_3)$ by He^{2+} ions, which are seen as a very prominent contribution to solar wind potential sputtering, was investigated. Thin films of $CaSiO_3$ deposited on a quartz crystal microbalance were irradiated allowing precise in-situ real time sputtering yield measurements. Experimental results were compared with simulations with the code SDTrimSP, which were improved by adapting the used surface binding energy.

On a freshly prepared surface He^{2+} ions show a significant increase in sputtering compared to equally fast He^+ ions. The yield, however, decreases exponentially with fluence, reaching steady state at considerably lower values after sputtering of the first few monolayers. Experiments using Ar^{8+} ions show a similar behavior and are qualitatively explained by a preferential depletion of surface oxygen due to potential sputtering. A corresponding quantitative model is applied, which is able to reproduce the observed potential sputtering behavior of both He and Ar very well. The results of these calculations support the assumption that mainly O atoms are affected by potential sputtering. We conclude that the defect-mediated model of potential sputtering is also well-suited for $CaSiO_3$.

1. Introduction

Ion-induced sputtering as part of space weathering is a key aspect to the erosion of planetary and moon surfaces due to solar wind ions that has to be investigated in detail (Hapke 2001). Laboratory sputtering experiments with mineral analogue targets are rare and therefore most models of space weathering and exosphere creation estimate sputtering yields or rely on numerically calculated values (see for example (Kallio & Janhunen 2003; Killen et al. 2007; Pfleger et al. 2015; Wurz et al. 2018; Wurz et al. 2007)). Numerical simulations are mostly performed with codes based on the binary collision approximation (BCA). In planetary sciences this is often done with TRIM simulations included in the SRIM package (Ziegler, Ziegler, & Biersack 2010). Especially for plasma-wall interaction in nuclear fusion reactors, dynamic BCA programs such as SDTrimSP (Mutzke et al. 2019) or TRI3DYN (Möller 2014) are more established. For example, N implantation in Be (Oberkofler et al. 2015) or chemical effects of C erosion as a result of H irradiation (Rai, Mutzke, & Schneider 2010) have successfully been modeled. Strong focus has recently been put on expanding BCA programs to include effects relevant for sputtering of rough surfaces or nanostructuring (see for example (Stadlmayr et al. 2018; Stadlmayr et al. 2019) or (Arredondo et al. 2019)).

However, some effects are not included in these simulations, such as the sputtering of insulating targets by the potential energy of multiply charged ions, termed "potential sputtering" (Aumayr & Winter 2004). During space weathering, potential sputtering is an additional contribution to the sputtering by He^{2+} and heavier multiply charged ions in the solar wind. Some investigations exist for the potential sputtering effects of the solar wind (Barghouty et al. 2011; Hijazi et al. 2017; Hijazi et al. 2014; Meyer et al. 2011), but in general experiments with relevant analogue minerals are lacking. To further investigate solar wind sputtering, we have performed corresponding irradiations on thin films deposited from wollastonite ($CaSiO_3$). Here the pyroxenoid wollastonite has been used as an analogue for the lunar surface. It can also be seen as an analogue to the general pyroxene contributions to bodies such as the Moon or Mercury, where pyroxene minerals (together with plagioclase) make up a significant amount of the respective surfaces (Cremonese et al. 2005; Yamashita et al. 2012). First results from these experiments can be found in a previous publication (Szabo et al. 2018). While kinetic sputtering for H^+ and Ar^+ was found to be in good agreement with SDTrimSP simulations, considerable potential sputtering contributions were observed for higher Ar charge states. Ar is only a minor constituent of the solar wind, but it is a suitable

analogue for the heavy ion contribution in the solar wind making it possible to get more insight of the fundamental physics of potential sputtering of minerals. A dependence of the potential sputtering yield on the ions' potential energy similar to Hijazi et al. was found (Hijazi, et al. 2017).

Significant deviations from the kinetic sputtering yield already occur for Ar^{2+} ions, which carry a potential energy of 41 eV (DREEBIT 2018). As a first assumption, potential sputtering should be independent of the ion species, just the potential energy should be important. Therefore, He^{2+} should cause an even higher potential sputtering since these ions carry a potential energy of 77 eV (DREEBIT 2018). He^{2+} is much more prominent in the solar wind than heavier ions and will probably play the most important role for potential sputtering (Wurz 2005). Previously we have used data from Ar^{q+} measurements to estimate the potential sputtering for He^{2+} ions to be about five times higher than the kinetic sputtering yield at the He solar wind energy of 4 keV (see Figure 1) (Szabo, et al. 2018). This would make He^{2+} the most significant source of solar wind sputtering. We have now performed experiments with singly and doubly charged He ions to verify whether our extrapolation really holds.
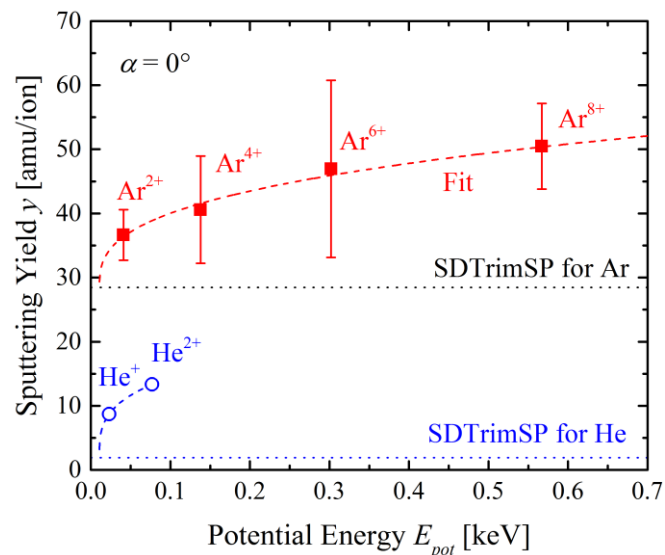

Figure 1: Measured sputtering yields for impact of 8 keV Ar^{q+} ($2 \leq q \leq 8$) ions on $CaSiO_3$ under normal incidence as a function of the ions' potential energy (red data points). Results from SDTrimSP are used to estimate the yield of kinetic sputtering (black dotted line). The potential sputtering contribution (difference between measured yields and results from SDTrimSP) can be fitted by the

formula $\alpha \times (E_{pot} - 2E_B)^\beta$ with twice the material's band gap as a threshold energy (Szabo, et al. 2018). This fit is used to extrapolate the expected potential sputtering yield for 4 keV He$^+$ and He^{2+} (open blue symbols, kinetic contribution again taken from SDTrimSP).

2. Methods

2.1   Experimental Setup

All presented sputtering experiments were performed with the same ion beam setup as described in Szabo et al. (Szabo, et al. 2018). Sputtering yields are measured with the Quartz Crystal Microbalance (QCM) technique (Hayderer et al. 1999a), which allows in-situ observation of thin film mass changes in real time by recording the resonance frequency of the quartz's thickness oscillation. Targets are mounted on a rotatable sample holder allowing measurements under different angles of incidence. Experiments at different temperatures are possible by heating the sample, however, all presented irradiations were performed at room temperature.

He irradiations were performed using both ^{4}He and ^{3}He at solar wind velocities of 1 keV/amu. ^{3}He had to be used to guarantee a clean He^{2+} ion beam that was not contaminated with molecular H_2 ions. Such a small H component of the ECR plasma has to be expected due to a source base pressure of 10^{-7} mbar. In the experimental setup at TU Wien, a magnetic sector field is used for mass-over-charge separation, which deflects ^{4}He^{2+} and H_2^+ in the same way making it impossible to isolate the He^{2+} ions due to their (almost) identical mass-over-charge-state ratio. During a current measurement, both ^{4}He^{2+} and H_2^+ would be registered and as a result, the total number of ^{4}He^{2+} ions would be overestimated. As H sputtering yields are an order of magnitude smaller than the expected He yields, already small but unavoidable H contaminations of the ion source would lead to errors in the measurement.

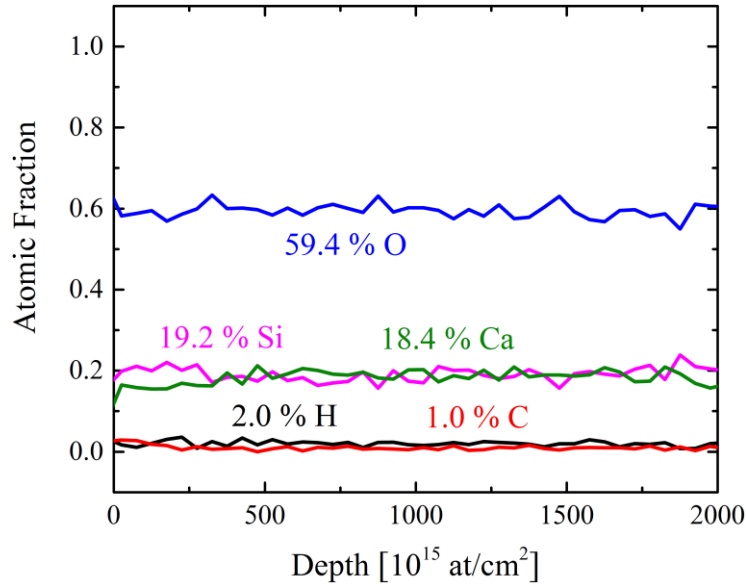### 2.2   Sample Preparation and Analysis

Figure 2: ToF-ERDA analysis of a 700 nm CaSiO$_3$ film for the first 2000 x 10^{15} at./cm^2 (roughly 260 nm), where this method can reliably probe the elemental sample composition.

Similar to the previous experiments (Szabo, et al. 2018), thin CaSiO$_3$ films deposited on our quartz crystals by Pulsed Laser Deposition (PLD) were used for the sputter yield measurements. The PLD was performed in 0.04 mbar O$_2$ atmosphere at a substrate temperature of ~270 °C with the laser operating at 5 Hz and a fluence of 2 J/cm^2 on the target for 60 minutes. The films were analyzed with Rutherford Backscattering Spectrometry (RBS) and Time-of-Flight Elastic Recoil Detection Analysis (ToF-ERDA), from which target thickness and depth dependent elemental concentrations could be obtained. RBS using a 2 MeV He beam showed that the target thicknesses of the films varied between 250×10^{15} at./cm^2 and 5300×10^{15} at./cm^2 depending on the PLD parameters (varying number of laser pulses). Assuming a film density similar to the nominal CaSiO$_3$ density, for which we use 2.86 g/cm^3 as the minimal reported measured value (Deer, Howie, & Zussman 1997), this corresponds to an actual film thickness between about 30 and 700 nm. ToF-ERDA analysis with 36 MeV iodine ions proves that the PLD films are very similar to the stoichiometric CaSiO$_3$ composition. Figure 2 shows the ERDA analysis of the 700 nm film as an example. Close to the surface, slightly less Ca than Si is observed, which is consistent with the sputter-XPS results for targets of the same batch (Szabo, et al. 2018). However, across the whole analyzed area the average composition is 18.4 % Ca, 19.2 % Si, 59.4 % O and only 2.0 % H

and 1.0 % C. Similar results were also found for the 30 nm film (18.3 % Ca, 20.0 % Si, 59.5 % O, 1.2 % H and 1.0 % C), showing that PLD provides good sample compositions also at low film thicknesses. Therefore we assume that the film composition is close to stoichiometric $CaSiO_3$ across the whole film.

2.3   Kinetic Sputtering Simulations

Kinetic sputtering yields were simulated with the BCA programs SDTrimSP and SRIM. In previous investigations, it was found that SDTrimSP can reproduce the angular dependence of Ar sputtering yields when taking into account the sample composition from XPS (Szabo, et al. 2018). There we also stated that the nominal $CaSiO_3$ composition leads to a significant overestimation of sputtering yields. However, the ToF-ERDA results in Figure 2 indicate that small deviations from the stoichiometric composition are only present at the surface. For prolonged sputtering experiments, they should not play a significant role and an agreement with a simulation using the stoichiometric $CaSiO_3$ composition should also be found.

For BCA simulations, especially the surface binding energies of the target elements play an important role. According to Sigmund's sputtering theory, the sputtering yield is inversely proportional to the surface binding energy (Sigmund 1969). In general, the heat of sublimation can be used as a good approximation for mono-elemental samples (Behrisch & Eckstein 2007), which are included as tabulated values in SRIM or SDTrimSP. However, for composite targets the surface binding energy usually represents an unknown quantity. Different theories have been developed to calculate these energies by using, for example, bond energies and electronegativity (Malherbe, Hofmann, & Sanz 1986), nearest-neighbor bond strengths (Kelly 1980) or the formation enthalpy (Möller & Posselt 2001). However, no universally accepted formalism for calculating unknown surface binding energies exists. Therefore, a common approach for a solid-gas compound is to keep the heat of sublimation for the solid elements and adapt the surface binding energy of the gaseous component to fit experimental results. Together with including the realistic density of $CaSiO_3$, this method was also applied for simulating the sputtering of $CaSiO_3$ leading to consistently good agreement with experimental results. The parameters used are described and justified in detail in the Supplementary Material.
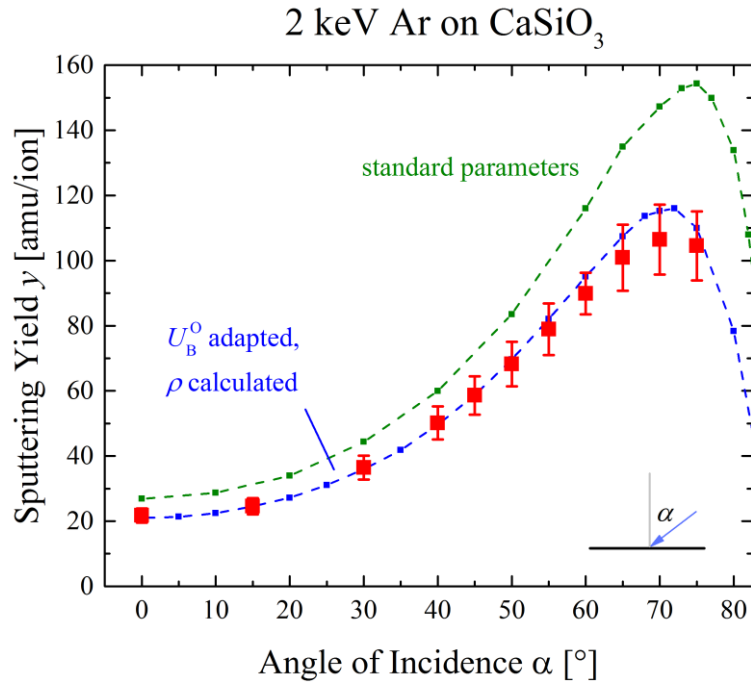
Figure 3: Comparison of different SDTrimSP simulations with experimental results (red) for 2 keV Ar sputtering yields. Standard parameters (green) overestimate the measured yields, while the new calculated density ρ and the adapted O surface binding energy U_B^O (blue) give a better agreement.

The result of simulating kinetic sputtering by 2 keV Ar ions are shown in Figure 3. The experimental values (red, taken from (Szabo, et al. 2018)) are compared to a simulation using standard parameters for SDTrimSP (green), leading to an overestimation of the experimental results. The more realistic target density and an adapted surface binding energy (see the Supplementary Materials) show improved agreement with the experiment (blue). In particular, lower sputtering yields result from the higher O surface binding energy. The plotted simulations were performed in the static mode of SDTrimSP. Dynamic simulations were done for selected angles using the adapted parameters, but there were only concentration changes of a few percent observed as well as no significant changes in the mass sputtering yield. These results are in line with experimental observations, where no substantial fluence dependence of the sputtering yield could be observed for the investigated

fluences in the order of 10^{19} ions/m^2. This set of parameters is therefore also used for the simulations of the kinetic sputtering contribution of He ions in the following sections.
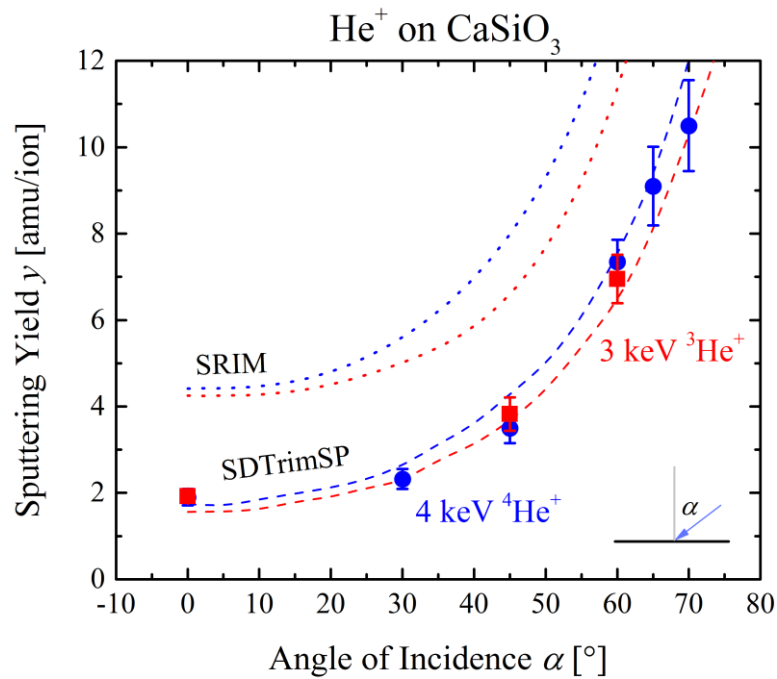
3. Sputtering Measurements

3.1 He$^+$ Sputtering

Figure 4: Comparison of the sputtering yields for 3 keV ^{3}He$^+$ (red) and 4 keV ^{4}He$^+$ (blue) bombardment. Experimental results are plotted for different angles of incidence together with simulation results from SDTrimSP (dashed lines) and SRIM (dotted lines).

First, sputtering with He$^+$ at approximate solar wind velocity (1 keV/amu) was investigated for 4 keV ^{4}He$^+$ and for 3 keV ^{3}He$^+$. ^{4}He is much more significant than ^{3}He in the solar wind, but as mentioned in Section 2.1 using ^{3}He was necessary for investigations with doubly charged He. At the beginning of He irradiations on fresh targets, a significant mass increase of the QCM caused by He implantation in the sample was observed. Fluences of about 1×10^{17} ions/cm^2 were necessary to reach steady state under 0° irradiation. Experimental

sputtering yields were obtained from this steady state value. Assuming constant sputtering during these irradiations until steady state, the observed implantation varied significantly. Over a predicted implantation depth of about 30 nm, the measured mass changes correspond to an implanted He concentration between 1% and 6%. For these concentrations, dynamic SDTrimSP simulations predict maximal sputtering yield reductions of 7% in the steady state compared to a simulation without He implantation. This value is close to the experimental uncertainties of the measured sputtering yields. Furthermore, dynamic SDTrimSP simulations in general do not show any significant sputtering yield changes due to preferential sputtering by prolonged He irradiation. Therefore, we conclude that the measured steady state yields are representative of He sputtering of $CaSiO_3$ regardless of any He implantation. Nevertheless, the exact interplay between He implantation and diffusion inside the sample causing the observed transient effect of the mass change is not yet fully understood.

Figure 4 shows the measured sputtering yields for ^{3}He$^+$ (red squares) and ^{4}He$^+$ (blue circles) under different angles of incidence (taken with respect to the surface normal). For all investigated angles, the measured sputtering yields for both He isotopes at the same impact velocity coincide within their uncertainty limits. The experimental results are plotted together with simulation results from SDTrimSP (dashed lines) and SRIM (dotted lines). Similar as observed for Ar sputtering, SRIM significantly overestimates experimental sputtering yields. SDTrimSP, on the other hand, precisely predicts sputtering yield in accordance with our findings for sputtering by Ar ions. Besides the absolute values, the simulation predicts the sputtering yields for the two He isotopes to be very similar at the same velocity, which agrees with experimental findings. As the ionization energies and therefore the potential energies are equal for both He isotopes, sputtering yield with 3 keV ^{3}He can be used to describe solar wind sputtering with ^{4}He.
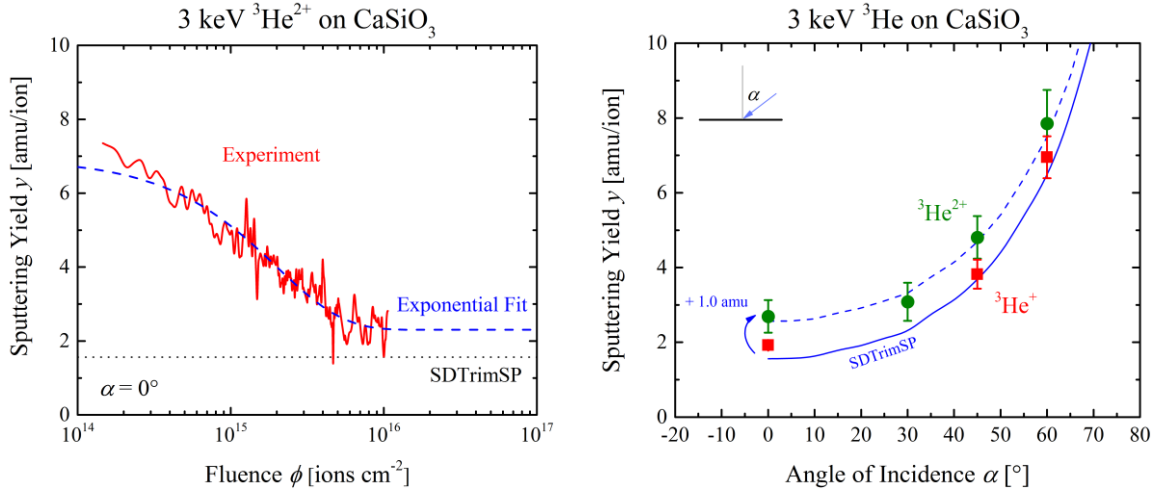
3.2 He^{2+} Sputtering

Figure 5: Left: Fluence dependence of the sputtering yield with continuous $^3He^{2+}$ bombardment at normal incidence. Right: Angular dependence of the ^3He sputtering yields in the steady state. Experimental results of $^3He^+$ (red) and $^3He^{2+}$ (green) are compared to SDTrimSP simulations.

Sputtering yields with $^3He^{2+}$ were measured for angles of incidence between 0° and 60° to investigate the influence of potential sputtering. In order to separate He^{2+} sputtering from implantation effects, the He^+ steady state under 0 degrees was taken as a starting point because no more He implantation should occur there. As it is shown in the left image in Figure 5, detailed measurements of the sputtering yield at the beginning of the irradiation show a significantly increased sputter yield of about 7 amu/ion under normal incidence. It has to be noted that recording of the sputtering yield was only possible after an already applied fluence of about 10^{14} ions/cm². Local heating of the quartz as a result of starting ion bombardment causes an additional frequency drift at the beginning of each measurement. During the irradiation, the yield exponentially decreases until a steady state is reached after a fluence of 10^{16} ions/cm² at a value much closer to the kinetic sputtering yield. From the total frequency change until the steady state fluence (the value of 1.0×10^{16} ions/cm² was chosen being five times the decay length of the exponential fit), a total mass decrease of about 32 $\times 10^{15}$ amu /cm² can be calculated. The atomic density of $CaSiO_3$ is 172×10^{15} amu /cm²/nm and therefore, steady state is reached within the sputtering of the first few monolayers when no further He implantation is assumed. The right image in Figure 5 shows a compilation of steady state sputtering yields at different angles of incidence compared to the $^3He^+$ measurements from Figure 4. For the steady state yields of $^3He^{2+}$ a constant difference of

about 1 amu/ion to the SDTrimSP prediction is observed for all investigated angles of incidence.

Similar fluence dependencies of potential sputtering were found in previous investigations of potential sputtering using SiO_2 (Varga et al. 1997), Al_2O_3 (Hayderer et al. 2001a) and MgO_x (Hayderer et al. 2001b) samples. In these studies this decrease of the sputtering yield was attributed to multiply charged ions causing a preferential sputtering of oxygen. Following the defect-mediated theory of potential sputtering, only O anions would desorb as a result of potential sputtering of an oxide target (Sporn et al. 1997). In this theory, an approaching ion that captures an electron from the insulating targets creates a localized electronic defect, a so-called self-trapped hole and self-trapped exciton, which subsequently leads to the desorption of neutral atoms (Hayderer et al. 1999b). Defect-mediated sputtering has been extensively investigated for alkali-halides showing precise agreement with the theory (Aumayr & Winter 2004; Hayderer, et al. 1999b; Neidhart et al. 1995; Wirtz et al. 2000). For other materials where no formation of localized defects has been reported, no potential sputtering was observed (Aumayr & Winter 2004). In the case of an oxide target, the self-trapped hole only affects the O anions and for electron irradiation of SiO_2 only O anion desorption is reported (Sporn, et al. 1997). Preferential O depletion by potential sputtering would then similarly cause a decrease in the surface O concentration for $CaSiO_3$ and therefore also a decrease of potential sputtering until a steady state is reached.

In the present work, identical initial conditions with a high potential sputtering yield could be reproducibly recreated in two ways: Either by sputter cleaning the sample's surface with Ar^+ ions or by oxygen flooding of the sample chamber (partial pressure of $10^{-3} - 10^{-4}$ mbar for several hours, both at room temperature or heated to 200°C). The first method corresponds to sputtering away the O-depleted layers, thus exposing a stoichiometric $CaSiO_3$ surface again, while the oxygen flooding re-oxidizes a depleted surface. The success of both methods is a strong indication that the qualitative explanation proposed by Hayderer et al. is indeed correct (Hayderer, et al. 2001a; Hayderer, et al. 2001b).
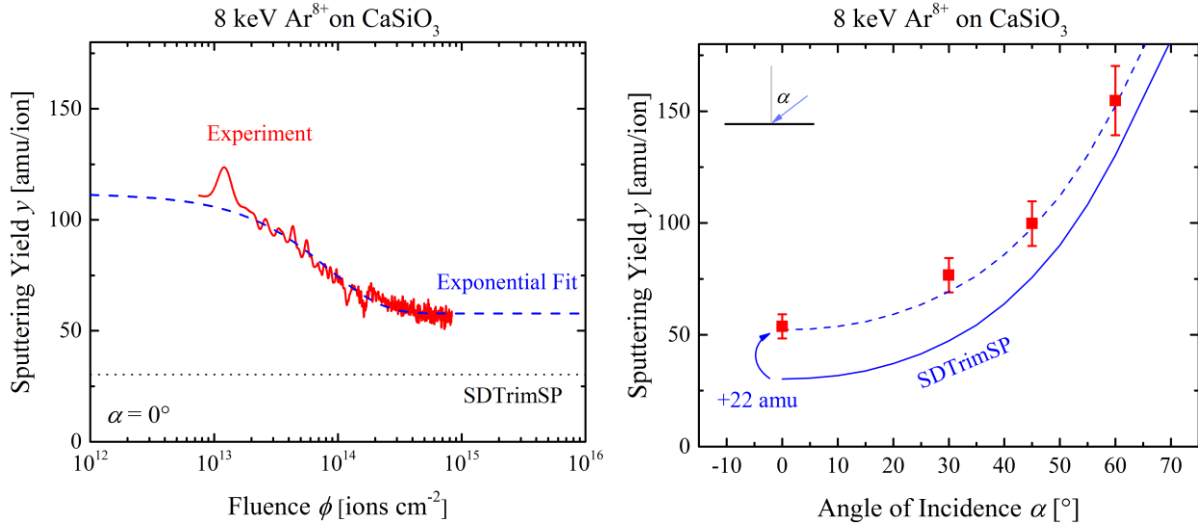

3.3 Ar Sputtering

Figure 6: Left: Fluence dependence of the sputtering yield under continuous Ar^{8+} irradiation. Right: Steady state sputtering yields of Ar^{8+} (red), which show a constant increase of 22 amu/ion compared to the SDTrimSP simulation for 8 keV Ar.

Fluence dependent sputtering yields were similarly found for Ar^{8+} measurements in a new, more detailed investigation presented in Figure 6. They also show an exponential decrease reaching steady state at fluences lower by a factor of 10 compared to ^{3}He. Constant increases compared to the kinetic sputtering yields are found for all angles, in this case 22 amu/ion (see the right image in Figure 6). The mass decrease up until a fluence of 4.3×10^{14} ions/cm^2 (five times the decay length of the exponential fit) is 29×10^{15} amu/cm^2. It is very similar to the observed value for ^{3}He irradiations and therefore steady state is again reached after sputtering the first few atomic monolayers. The similar exponential decrease would also support the assumption of O depletion and therefore smaller potential sputtering effects.

Changing O sputtering yields were investigated by Meyer et al. for Ar sputtering of lunar regolith simulant using a quadrupole mass spectrometer approach (Meyer, et al. 2011). In this study no significant changes were observed, but with their reported high beam fluxes of 10^{14} – 10^{15} ions/s/cm^2, it might be difficult to observe the pre-steady-state phase. Even if potential sputtering only affects O atoms, a complete depletion of surface O would not be expected because kinetic sputtering will erode Ca and Si atoms and thus expose fresh O at the receding surface. Therefore, a lower than initial but non-zero surface O concentration should be

13

present in the equilibrium and the observed constant O sputter yields by Meyer et al. would be in agreement with this explanation.
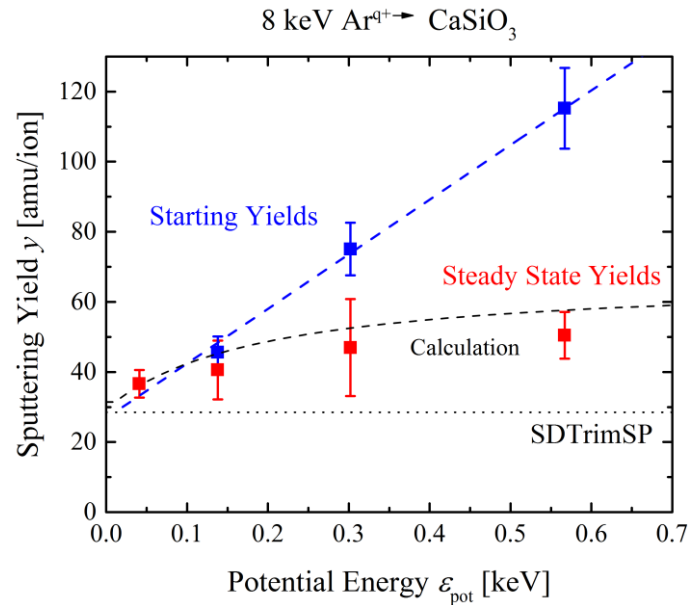

Figure 7: Ar sputtering yields for different potential energies of the ions, measured for the charge states 2+, 4+, 6+ and 8+. Sputtering yields at the beginning of the irradiation show a linear dependence (blue) with E_{pot}. Steady state yields are much less dependent on E_{pot} (red). The calculation for dynamic potential sputtering (black dashed line, see Section 4) is able to reproduce the measured steady state yields very well.

Using both of the described in-situ sample preparation methods, initial sputtering yields (i.e. sputter yields at the beginning of the irradiation) were measured, and the results are shown in Figure 7. The black dotted line represents results from an SDTrimSP simulation and is used as a reference for kinetic sputtering by 8 keV Ar ions. The difference between this value and the measured sputtering yield is attributed to potential sputtering. For Ar charge states up to 8+ the potential sputtering yield is then proportional to the ion's potential energy (see the dashed blue line in Figure 7). Its slope $\gamma_{Ar} \approx 9.7$ O atoms/keV or 155.2 amu/keV gives the dependence of the potential sputtering yield on the ion's potential energy, which will later be used to calculate potential sputtering effects numerically (see Section 4, Equation 4.4). Sporn et al investigated this dependence for potential sputtering of SiO_2 using multiply charged Ar

and Xe ions (Sporn, et al. 1997). There they found that the sputtering yields increase with 1 SiO_2 per 500 eV potential energy. This corresponds to 120 amu/keV and is therefore close to our findings for Ar^{q+} on $CaSiO_3$. However, the initial sputtering yield of $^3He^{2+}$ that is shown in Figure 5 does not fit the same dependence. To describe the initial value of ~ 7 amu/ion, a different slope $\gamma_{He} \approx 4.4$ O atoms/keV (70 amu/keV) has to be used.

Figure 7 also shows the measured yields from Szabo et al. in red (Szabo, et al. 2018). As they were measured multiple times to achieve better statistics, but without any oxidization or sputter cleaning in between, they have to be interpreted as steady state sputtering yields. These steady state yield were re-investigated for the present publication and agree with the previously published values.

4. Dynamic Sputtering Model

4.1 Theoretical Model

The previously shown measurements open up several questions that have yet to be answered quantitatively. It is necessary to investigate whether preferential sputtering of oxygen can explain the fluence dependence of potential sputtering. Furthermore, different steady state behaviors between He and Ar could also be explained in connection to this process due to the different kinetic sputtering yields. While potential sputtering presumably only erodes O atoms from $CaSiO_3$, a higher kinetic sputtering also causes additional removal of Ca and Si. This would bring more O to the surface leading to higher potential sputtering yields in the steady state.

To investigate if this qualitative assumption reproduces the previously shown measurements, a model for the dynamic sputtering consisting of a system of coupled differential equations was applied. A similar model has been used by Barghouty et al. and Alnussirat et al. to extrapolate changes of surface compositions of lunar soil simulants due to solar wind sputtering from measured sputtering yields (Alnussirat et al. 2018; Barghouty, et al. 2011). The coupled differential equations are as follows:

$$\frac{dC_{Ca}(\phi)}{d\phi} = \frac{1}{n_A}\left[-Y_{Ca}(\phi) + C_{Ca}^b \cdot \left(\sum_i Y_i(\phi)\right)\right]$$

$$\frac{dC_{Si}(\phi)}{d\phi} = \frac{1}{n_A}\left[-Y_{Si}(\phi) + C_{Si}^b \cdot \left(\sum_i Y_i(\phi)\right)\right] \quad (3.1)$$

$$\frac{dC_O(\phi)}{d\phi} = \frac{1}{n_A}\left[-Y_O(\phi) + C_O^b \cdot \left(\sum_i Y_i(\phi)\right)\right]$$

The surface concentration C_i of element i represents the relative concentration of the top monolayer, with n_A being the number of atoms per monolayer of 1.763×10^{15} at./cm^2 for CaSiO$_3$. Its change over fluence ϕ is made up from two parts: (1) Each incoming ion sputters a mean number of Y_i atoms, which decreases the surface concentration of element i. (2) Any sputtered surface atom can be replaced by a bulk atom of element i with a probability that is equal the bulk concentration C_i^b (as an approximation, changes to the concentration of deeper layers are neglected here). This process increases C_i and is described by the second term in brackets. There the sum of sputtering yields with index i is taken over all target elements.

The kinetic sputtering yield Y_i^{kin} of element i is taken from the CaSiO$_3$ sputtering yield simulated with SDTrimSP $Y_i^{SDTrimSP}$ and rescaled with the fluence dependent concentration:

$$Y_i^{kin}(\phi) = Y_i^{SDTrimSP} \cdot \frac{C_i(\phi)}{C_i^b} \quad (3.2)$$

Therefore, the system of differential equations (4.1) is coupled via the sputtering yields as they are proportional to the respective element concentrations $C_i(\phi)$.

For Ca and Si only kinetic sputtering is calculated, while O sputtering is assumed to be the sum of a kinetic and a potential contribution:

$$\begin{aligned} Y_{Ca} &= Y_{Ca}^{kin} \\ Y_{Si} &= Y_{Si}^{kin} \\ Y_O &= Y_O^{kin} + Y_O^{pot} \end{aligned} \quad (3.3)$$

For the potential sputtering yield, the following ansatz is taken based on the observed linear dependence of sputtering yields on potential energy (see Figure 7):

$$Y_O^{pot}(\phi) = \gamma \cdot \frac{C_O(\phi)}{C_O^b} \cdot \left(E_{pot} - 2E_B \right) \tag{3.4}$$

The potential sputtering yield in O atoms/ion is here proportional to the surface O concentration C_O and the ion's potential energy E_{pot} minus twice the material's band gap E_B, which was kept as the potential sputtering threshold from Hijazi et al. and Szabo et al. (Hijazi, et al. 2017; Szabo, et al. 2018). The parameter γ describes how efficiently potential energy can cause desorption of O atoms and can be calculated from the measurement of the initial sputtering yields (see Figure 7). As mentioned in Section 3, for Ar and He different parameters γ had to be taken ($\gamma_{Ar} \approx 9.7$ [O atoms/keV] and $\gamma_{He} \approx 4.4$ [O atoms/keV]). The oxygen sputtering yield is then the sum of kinetic and potential contributions:

$$Y_O(\phi) = Y_O^{kin}(\phi) + Y_O^{pot}(\phi) \tag{3.5}$$

$Y_O^{kin}(\phi)$ and $Y_O^{pot}(\phi)$ are taken from equations (3.2) and (3.4).

The total sputtering yield y in amu/ion, which is the quantity measured with a QCM setup, is calculated by summing up the products of elemental sputtering yields Y_i and atomic masses m_i:

$$y(\phi) = Y_{Ca}(\phi) \cdot m_{Ca} + Y_{Si}(\phi) \cdot m_{Si} + Y_O(\phi) \cdot m_O \tag{3.6}$$

The system of differential equations was solved numerically with Wolfram Mathematica 11.2 to calculate the fluence dependent surface concentrations. With these quantities the fluence dependent sputtering yields and steady state conditions can also be obtained. In the next sections, the focus will be put on comparing steady state measurements with the corresponding sputtering yields $\lim_{\phi \to \infty} y(\phi)$.
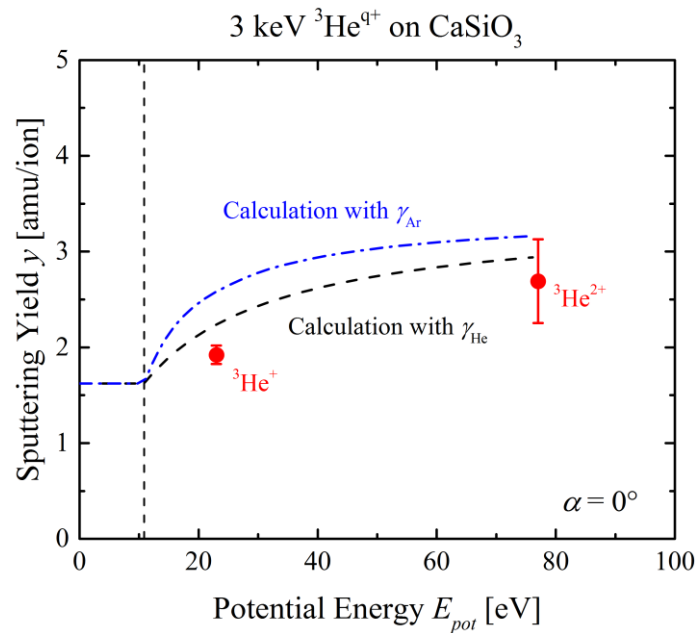
4.2 Results for He Sputtering Yields

Figure 8: Comparison of the steady state yields for ^{3}He sputtering plotted over the ion's potential energy. Measured yields (red) are compared to calculation results using the initial ^{3}He^{2+} yield from Figure 5 (black dashed line) or the initial Ar^{q+} yields from Figure 7 (blue dash-dotted line).

Using the model introduced in section 4.1, the steady state sputtering yields for He^{2+} can be well reproduced, as can be seen in Figure 8. There the black dashed line shows the results when the parameter γ_{He} of the measured initial ^{3}He^{2+} sputtering yield is used. For He^{2+}, potential sputtering plays an important role in preferentially sputtering O and due to the O depletion (see Figure 9 in Section 4.4) the sputtering yield decreases in good agreement with the experiment. However, sputtering yields in Figure 8 (and the steady state O concentrations in Figure 9) show that already the potential energy of He$^+$ (24 eV) is high enough to cause changes in the target surface elemental composition. He^{2+} yields have always been recorded after sufficient He$^+$ bombardment to avoid complications due to He implantation (see section 3.1). But if He$^+$ already causes preferential O depletion, this could explain lower measured He^{2+} initial yields (i.e. an underestimation of the parameter γ). Therefore, a calculation with the parameter γ_{Ar} taken from the initial Ar yields, which is more than two times higher but would represent a universal potential sputtering for the different ions, is included in Figure 8

as the blue dash-dotted line. Despite large differences in the input both curves are close to the experimental finding for He^{2+}. The small differences occur because of potential sputtering initially dominating over kinetic sputtering for both calculations. This results in significant depletion of surface O, where changes in potential sputtering yields have little influence on the steady state. However, differences between γ_{Ar} calculation and the measured He^+ yield are quite significant and agree much better for the γ_{He} calculation. Varying values for γ_{Ar} and γ_{He} could be explained by the phenomenon of kinetically assisted potential sputtering, which was observed previously for MgO_x samples (Hayderer, et al. 2001b). Here potential sputtering was found to be proportional to the kinetic energy of the impacting ion (in addition to the potential energy), which would be in accordance with the different He and Ar energies.

Analysis of our calculations show that different surface binding energy models and possible variations in the target composition noticeably affect the outcome. Due to these uncertainties, no definitive recommendation can be given about which of the two γ parameters should be used because the steady state behavior of He^{2+} can be described well in both cases. Nevertheless, total agreement for γ_{He} is better, which is why the He calculations in the following sections show results based on γ_{He} potential sputtering.

4.3 Results for Ar Sputtering Yields

The calculation is also very well able to reproduce how the initial linear curve with E_{pot} (see Figure 7) develops into a much less pronounced dependence for the steady state yield on the ion's potential energy. As a comparison with the experimental yields, the calculated steady state yields are included in Figure 7 as the dashed black line. Even though a simple model was used for the calculation, the absolute values of the calculated steady state yields agree very well with all measured Ar charge states.

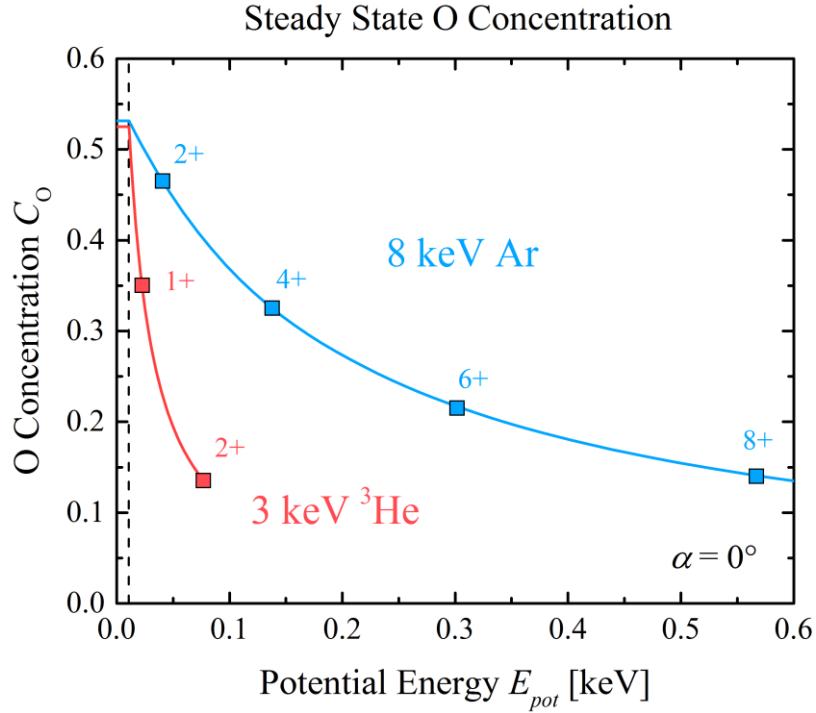*4.4 Steady State Oxygen Concentrations*

19

Figure 9: Calculated steady state O concentrations for normal incidence irradiation are plotted over the ion's potential energy. For Ar (blue), kinetic sputtering brings more O to the surface by eroding Ca and Si. For He (red), potential sputtering is dominant already at lower potential energy and O depletion is much more significant.

With our model we have successfully linked different behaviors of potential sputtering in cases of He and Ar bombardment to the depletion of surface O. The steady state O concentration is shown in Figure 9 for He (red, using γ_{He}) and Ar (blue) charge states. For He, potential sputtering is dominant at the beginning of the irradiation causing a strong depletion of surface O. As the potential sputtering is assumed to be proportional to the O concentration, its contribution is smaller than expected in the steady state when compared to kinetic sputtering alone (see the comparison between steady state yield and SDTrimSP simulations in Figure 5). In contrast, for Ar irradiation kinetic sputtering plays an important role in exposing fresh bulk O atoms at the surface. Ca and Si are sputtered more efficiently than by He ion impact, which leads to a higher O concentration in the steady state. Therefore, higher differences can be observed between experimental steady state yields including potential sputtering and the kinetic sputtering yield alone (see Figure 6).

Consequently, kinetic and potential sputtering in the steady state cannot be treated independently, but their interplay is important to understand the development of the sputtering yield.

5. Summary and Conclusion

Sputtering yields of $CaSiO_3$ were measured under irradiation with singly and doubly charged He ions at solar wind velocity. For He^+ the two isotopes $^3He^+$ and $^4He^+$ show identical sputtering yields when measured at equal impact velocity. Therefore, data obtained for sputtering with 3 keV ^3He can represent the ^4He contribution of the solar wind, because both kinetic sputtering and potential energies are equal. Measured sputtering yields agree very well with SDTrimSP simulations, after adapting the O surface binding energy. For He^{2+}, high initial potential sputtering yields could be observed, which are followed by an exponential decrease until a steady state is reached after the removal of a few monolayers of material. This behavior is consistent with new, more detailed 8 keV Ar^{8+} measurements and indicates a strong depletion of surface O due to potential sputtering. Using in-situ re-prepared surfaces, Ar sputtering yields at the beginning of the irradiation were found to have a linear dependence on the ion's potential energy.

A model with a set of coupled differential equations was applied to calculate the effects of He and Ar sputtering, assuming a potential sputtering yield that is linearly dependent on the surface O concentration and the ion's potential energy. This model is able to explain how the observed (initial) linear energy dependence turns into much less pronounced changes for higher potential energies in the steady state case. Absolute values for the steady state sputtering yields can be reproduced very well for both He and Ar ions. The calculation therefore indicates that the assumption of only O atoms being potentially sputtered is reasonable and potential sputtering of $CaSiO_3$ proceeds according to the defect-mediated sputtering model. The development of the sputtering yield during the irradiation is dominated by the interplay of kinetic and potential sputtering, leading to significant differences in He and Ar yields. Kinetic sputtering plays an important role to increase the surface O concentration in the steady state, which in turn causes a rise in potential sputtering.
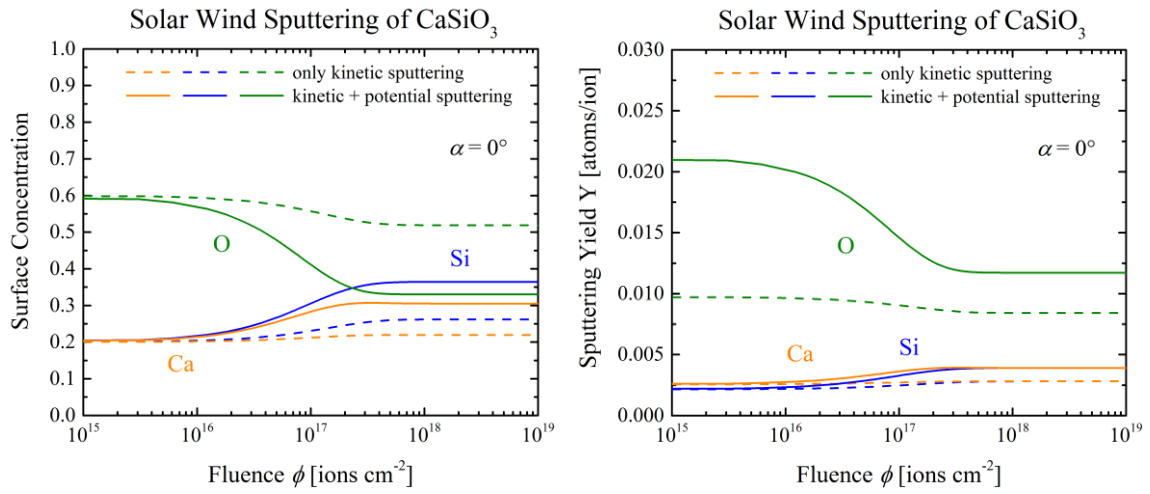
Figure 10: Left: Fluence dependence of the calculated surface concentration changes resulting from solar wind sputtering of CaSiO₃, assuming a solar wind composition of 96% H and 4% He. Dashed lines represent the concentrations for Ca (orange), Si (blue) and O (green) with kinetic sputtering only. Full lines include both kinetic sputtering of H and He as well as potential sputtering by He^{2+} ions. Right: Depiction of the fluence dependence of the respective sputtering yields under 96% H, 4% He solar wind bombardment. In the steady state case potential sputtering increases all yields by about 40%.

The interplay of kinetic and potential sputtering is also very important for the solar wind in general, where mainly H^+ and He^{2+} bombard mineral surfaces of atmosphere-less bodies at the same time. The solar wind protons will increase the kinetic erosion and are therefore also indirectly responsible for higher potential sputtering yields. Figure 10 shows the results from a simulation of these effects by modelling solar wind sputtering with 96% H^+ and 4% He^{2+} (Russell, Luhmann, & Strangeway 2016). The changes of the surface concentrations for Ca (orange), Si (blue) and O (green) as a result of ion sputtering are plotted over ion fluence on the left image, while the right image shows the development of the respective yields. Two calculations are compared: dashed lines represent modelling of only kinetic sputtering effects, while full lines include potential sputtering by He^{2+} ions. A clear O depletion to a surface concentration of about 30% is predicted as a result of potential sputtering. On the other hand, all sputtering yields are increased by including the potential sputtering effects because of the change in surface concentration. In the steady state, where the ratio between yields represents

the bulk ratio, all sputtering yields are increased by 39% compared to kinetic sputtering only. Pure H sputtering would be lower by another 20% making the total difference between H and H+He sputtering 67%. Similar to recent previous work on solar wind sputtering (see for example (Hijazi, et al. 2017) or (Szabo, et al. 2018)), our results underline the importance of including at least He^{2+} to solar wind modelling. Further (but smaller) effects are then to be expected by heavier, multiply charged ions.

Our experimental results have been consistently verified by modelling O desorption as a result of potential sputtering, based on the defect-mediated model of potential sputtering and previous experimental findings. Nevertheless, future experiments should aim to verify the predicted O depletions with in-situ sample analysis. In space, O reduction has been observed on the Moon, where the darkening and reddening of the lunar surface has been connected to the formation of nanophase Fe particles assumed to originate via disassociation from regolith minerals (Kohout et al. 2014; Pieters & Noble 2016). Even though micrometeorite impacts are expected to significantly contribute to the formation of such nanoparticles (Sasaki et al. 2001), these observations support that O depletion by potential sputtering plays a role during space weathering.

Another aspect that should be taken into account for future experiments is how different temperatures affect potential sputtering. As can be seen in Figure 10, steady state for H+He sputtering is reached after a fluence of about 10^{18} ions/cm^2, which corresponds to a time in the order of 100 years for a solar wind flux at the Moon of about 10^8 ions/ cm^2 (Russell, et al. 2016). This is a short time on an astronomical scale, but for elevated surface temperatures diffusion will affect the surface concentrations. This could affect space weathering on the Moon (up to 400 K), but should especially be a concern for Mercury's expected maximum temperatures of 700 K (Vasavada, Paige, & Wood 1999). It has to be checked whether this will bring more O to the surface, which would lead to an even more pronounced role of potential sputtering.

 Solar wind sputtering research would also greatly benefit from improvements in simulations. While the presented model works very well in reproducing sputtering yields, some limitations have become apparent. For example, the model overestimates the fluence needed until steady state for both He (by a factor of 2) and Ar (by a factor of 5). In the case of Ar irradiation, several keV of kinetic energy are deposited within a few nanometers underneath the surface. Surface O depletion would therefore be affected by intermixing of atomic layers in the

collision cascade. This is an effect that goes beyond the presented calculations. Including some potential sputtering effects in already established BCA codes, similar as it is done for chemical sputtering of C in SDTrimSP (Mutzke, et al. 2019), would therefore significantly enhance simulations of cases relevant for solar wind sputtering.

Acknowledgments

References

Alnussirat, S. T., Barghouty, A. F., Edmunson, J. E., Sabra, M. S., & Rickman, D. L. 2018, Nuclear Instruments and Methods in Physics Research Section B: Beam Interactions with Materials and Atoms, 420, 33

Arredondo, R., et al. 2019, Nuclear Materials and Energy, 18, 72

Aumayr, F., & Winter, H. 2004, Philosophical Transactions of the Royal Society of London A: Mathematical, Physical and Engineering Sciences, 362, 77

Barghouty, A. F., Meyer, F. W., Harris, P. R., & Adams, J. H. 2011, Nuclear Instruments and Methods in Physics Research Section B: Beam Interactions with Materials and Atoms, 269, 1310

Behrisch, R., & Eckstein, W. 2007, Sputtering by Particle Bombardment: Experiments and Computer Calculations from Threshold to MeV Energies (Springer Science & Business Media)

Cremonese, G., Bruno, M., Mangano, V., Marchi, S., & Milillo, A. 2005, Icarus, 177, 122

Deer, W. A., Howie, R. A., & Zussman, J. 1997, Rock-forming minerals: single-chain silicates, Volume 2A

DREEBIT. 2018, DREEBIT - Ionization Energy Database

Hapke, B. 2001, Journal of Geophysical Research: Planets, 106, 10039

Hayderer, G., et al. 2001a, Nuclear Instruments and Methods in Physics Research Section B: Beam Interactions with Materials and Atoms, 182, 143

Hayderer, G., et al. 2001b, Physical Review Letters, 86, 3530

Hayderer, G., Schmid, M., Varga, P., Winter, H. P., & Aumayr, F. 1999a, Review of Scientific Instruments, 70, 3696

Hayderer, G., et al. 1999b, Physical Review Letters, 83, 3948

Hijazi, H., Bannister, M., Meyer, H., Rouleau, C. M., & Meyer, F. 2017, Journal of Geophysical Research: Planets, 122, 1597

Hijazi, H., Bannister, M. E., Meyer, H. M., Rouleau, C. M., Barghouty, A. F., Rickman, D. L., & Meyer, F. W. 2014, Journal of Geophysical Research: Space Physics, 119, 8006

Kallio, E., & Janhunen, P. 2003, Geophysical Research Letters, 30

Kelly, R. 1980, Surface Science, 100, 85

Killen, R., et al. 2007, Space Science Reviews, 132, 433

Kohout, T., et al. 2014, Icarus, 237, 75

Malherbe, J., Hofmann, S., & Sanz, J. 1986, Applied Surface Science, 27, 355

Meyer, F. W., Harris, P. R., Taylor, C. N., Meyer III, H. M., Barghouty, A. F., & Adams, J. H. 2011, Nuclear Instruments and Methods in Physics Research Section B: Beam Interactions with Materials and Atoms, 269, 1316

Möller, W. 2014, Nuclear Instruments and Methods in Physics Research Section B: Beam Interactions with Materials and Atoms, 322, 23

Möller, W., & Posselt, M. 2001, in TRIDYN User Manual

Mutzke, A., Schneider, R., Eckstein, W., Dohmen, R., Schmid, K., Toussaint, U. v., & Badelow, G. 2019, in IPP-Report

Neidhart, T., Pichler, F., Aumayr, F., Winter, H., Schmid, M., & Varga, P. 1995, Physical Review Letters, 74, 5280

Oberkofler, M., et al. 2015, Fusion Engineering and Design, 98, 1371

Pfleger, M., et al. 2015, Planetary and Space Science, 115, 90

Pieters, C. M., & Noble, S. K. 2016, Journal of Geophysical Research: Planets, 121, 1865

Rai, A., Mutzke, A., & Schneider, R. 2010, Nuclear Instruments and Methods in Physics Research Section B: Beam Interactions with Materials and Atoms, 268, 2639

Russell, C. T., Luhmann, J. G., & Strangeway, R. J. 2016, Space Physics: An Introduction (Cambridge University Press)

Sasaki, S., Nakamura, K., Hamabe, Y., Kurahashi, E., & Hiroi, T. 2001, Nature, 410, 555

Sigmund, P. 1969, Physical Review, 184, 383

Sporn, M., et al. 1997, Physical Review Letters, 79, 945

Stadlmayr, R., et al. 2018, Nuclear Instruments and Methods in Physics Research Section B: Beam Interactions with Materials and Atoms

Stadlmayr, R., Szabo, P. S., Mayer, D., Cupak, C., Möller, W., & Aumayr, F. 2019, Physica Scripta

Szabo, P. S., et al. 2018, Icarus, 314, 98

Varga, P., Neidhart, T., Sporn, M., Libiseller, G., Schmid, M., Aumayr, F., & Winter, H. 1997, Physica Scripta, 1997, 307

Vasavada, A. R., Paige, D. A., & Wood, S. E. 1999, Icarus, 141, 179

Wirtz, L., et al. 2000, Surface science, 451, 197

Wurz, P. 2005. in The Dynamic Sun: Challenges for Theory and Observations, Solarwind composition

Wurz, P., Gamborino, D., Vorburger, A., & Raines, J. 2018, Journal of Geophysical Research: Space Physics, 124, 2603

Wurz, P., Rohner, U., Whitby, J. A., Kolb, C., Lammer, H., Dobnikar, P., & Martín-Fernández, J. A. 2007, Icarus, 191, 486

Yamashita, N., et al. 2012, Earth and Planetary Science Letters, 353, 93

Ziegler, J. F., Ziegler, M. D., & Biersack, J. P. 2010, Nuclear Instruments and Methods in Physics Research Section B: Beam Interactions with Materials and Atoms, 268, 1818